On the Characterization of Membrane Transport Phenomena and Ion Exchange Capacity for Non-Aqueous Redox Flow Batteries

Journal of The Electrochemical Society

OPEN ACCESS

On the Characterization of Membrane Transport Phenomena and Ion Exchange Capacity for Non-Aqueous Redox Flow Batteries

Journal of The Electrochemical Society, 2022 **169** 080528

On the Characterization of Membrane Transport Phenomena and Ion Exchange Capacity for Non-Aqueous Redox Flow Batteries

Rémy Richard Jacquemond,[1,2] Rosa Geveling,[1] Antoni Forner-Cuenca,[1,*] and Kitty Nijmeijer[1,2,z]

[1]*Membrane Materials and Processes, Department of Chemical Engineering and Chemistry, Eindhoven University of Technology, 5600 MB Eindhoven, The Netherlands*
[2]*DIFFER - Dutch Institute for Fundamental Energy Research, 5600 HH5612 Eindhoven, The Netherlands*

The development of high-performance membrane materials for non-aqueous redox flow batteries (NAqRFBs) could unlock a milestone towards widespread commercialization of the technology. Understanding of transport phenomena through membrane materials requires diagnostic tools able to monitor the concentrations of redox active species. While membrane characterization in aqueous media focused the attention of the scientific community, dedicated efforts for non-aqueous electrolytes remain poorly developed. Here, we develop new methodologies to assess critical membrane properties, namely ion exchange capacity and species transport, applied to NAqRFBs. In the first part, we introduce a method based on ^{19}F-NMR to quantify ion exchange capacity of membranes with hydrophobic anions commonly used in non-aqueous systems (e.g., PF_6^- and BF_4^-). We find a partial utilization of the ion exchange capacity compared to the values reported using traditional aqueous chemistry ions, possibly limiting the performance of NAqRFB systems. In the second part, we study mass transport with a microelectrode placed on the electrolyte tank. We determine TEMPO crossover rates through membranes by using simple calibration curves that relate steady-state currents at the microelectrode with redox active species concentration. Finally, we show the limitations of this approach in concentrated electrolyte systems, which are more representative of industrial flow battery operation.
 [DOI: 10.1149/1945-7111/ac8623]

Manuscript submitted May 20, 2022; revised manuscript received July 6, 2022. Published August 25, 2022. *This paper 119, was presented during the 240th Meeting of the Electrochemical Society, October 10–14, 2021.*

Supplementary material for this article is available online

General background of redox flow batteries (RFBs).—Efficient and reliable large scale energy storage systems will play a central role in the transition to a sustainable society by facilitating the storage of energy produced from renewable sources (e.g. solar and wind).[1,2] Integrating energy storage systems into the grid network needs to be economically viable and the U.S. Department of Energy (DOE) set a cost target between $100 and $150/kWh for stationary electricity storage.[3–7] Among the available technologies, RFBs are promising owing to their design flexibility accommodating for different energy needs without drastically increasing the capital cost.[3,8,9] RFBs are electrochemical systems reversibly converting chemical energy into electrical energy via redox reactions. A typical RFB system is composed of external tanks storing the electrolyte solutions (catholyte and anolyte) and an electrochemical stack with porous electrodes separated by a membrane. During operation, redox active molecules stored in the tanks are pumped through the porous electrodes and undergo redox reactions, providing electrons to power a load. An ideal membrane assures selective separation between the cathodic and anodic compartments of the battery and allows permeation of the desired charge carrying species balancing the half-cells electroneutrality while preventing the passage of the redox active molecules. In practice, membranes are never perfectly selective between desired and non-desired ion transport which of course decreases the performance of the battery. The standard redox potentials of the catholyte and anolyte materials determine the open circuit voltage (OCV) of the RFB, however cell inefficiencies during operation result in lower operating voltage.[10] Electrochemical cells suffer from kinetic, mass transport and ohmic overpotentials whose respective contributions vary depending on the RFB electrolyte composition and cell-architecture. The ohmic overpotential is significantly affected by the membrane as it corresponds to a zone of low conductivity within the cell, its ohmic contributions also scales with the electrolyte ionic conductivity. The energy capacity of the RFB is defined by the amount of redox active species in the electrolyte tanks while the power density is determined by the design of the cell stacks. Therefore, the energy capacity and the power can be scaled independently, making RFBs suitable to cover a range of energy needs.

Aqueous redox flow batteries.—The early RFBs focused on aqueous electrolytes development, often using corrosive chemicals with scarce metals as redox active materials (e.g., all-vanadium and iron-chromium RFBs are commercialized and deployed at the MW/MWh scale). Additionally, water is a convenient solvent to use in batteries as it is a good ionic conductor, cheap, non-toxic and non-flammable. However, aqueous operation of any electrochemical storage device has its energy density intrinsically restricted by the electrochemical stability window of water (1.23 V under standard conditions). Another factor limiting the energy density is the solubility of the transition metal-based redox active species which are generally soluble up to 2 M.[11] Vanadium RFBs attracted most of the attention over the past decades and became the state-of-the-art in the technology. Some research is still ongoing on how to limit performance losses.[12,13]

Non-aqueous redox flow batteries.—In pursuit of systems with higher energy and power densities, non-aqueous redox flow batteries (NAqRFBs) have become attractive. Although NAqRFBs must overcome some challenges related to their low ionic-conductivity and toxicity, organic active molecules in non-aqueous electrolytes offer a vast range of design possibilities. Redox potentials of active molecules can be tailored through molecular engineering using cheap and abundant elements, organic solvents offer a broader electrochemical stability window, and they are stable under a wider working temperature range compared to water based electrolytes.[7,14] For example, propylene carbonate has a stability window higher than 6 V with reported active material solubilities as high as 7 M (quinoxaline).[15,16] Wider operating voltage and higher active species concentration result in superior energy density. Despite these

*Electrochemical Society Member.
[z]E-mail: d.c.nijmeijer@tue.nl

advantages, NAqRFBs did not receive significant attention for large-scale deployment yet. This is partly due to ohmic losses through the electrolyte and membrane, limiting the current and power densities to values still lower than those of their aqueous counterparts.[17]

Role and limitations of membranes in RFB systems.—In a redox flow cell, the membranes must provide two critical functions, namely promoting fast passage of ions, and preventing crossover of active species (n.b., only if the active species are not the charge carriers) that would result in capacity fade and a reduced coulombic efficiency. One possible strategy limiting the RFB capacity fade overtime is to use premixed electrolytes to lower the concentration-gradient-driven crossover.[18] Polymer membranes can be classified in porous separators and dense ion-exchange membranes (IEMs). Porous separators are generally polymer or ceramic materials with defined pores. These are cheap and highly conductive but generally give rise to fast crossover of redox active species. On the other hand, IEMs are dense charged polymeric matrices that can be either cation-exchange membranes or anion-exchange membranes (anion exchange membranes). NAqRFBs can be operated with both cation exchange membranes and anion exchange membranes but, in practice, anion exchange membranes are more studied because of the higher conductivity of common non-aqueous anions (e.g., BF_4^- or PF_6^-).[17] Lowering the internal ohmic losses is a major challenge to operate NAqRFBs at high current densities. The development of tailor-made membranes for non-aqueous applications is not trivial, forcing researchers to rely on commercial membranes initially designed for aqueous systems. The behavior of IEMs in organic solvents and the relation between membrane properties and NAqRFBs performance is still poorly understood, primarily due to the lack of systematic studies and adequate membrane characterization techniques tailored for RFB applications. Specifically, two membrane properties, i.e. ion exchange capacity and species crossover, remain poorly understood in NAqRFBs, which is the focus of our work.

Ion exchange capacity (IEC) of ion exchange membranes.—An important membrane property that has been extensively studied in aqueous systems but widely overlooked when employed in organic solvents is the ion exchange capacity. The IEC represents the number of ionogenic (fixed charge) groups contained in a "specific amount" of the material and can be calculated using Eq. 1.

$$IEC = \frac{number\ of\ fixed\ charges\ (meq)}{dry\ membrane\ weight\ \textbf{after ion exchange}\ (g)} \qquad [1]$$

The IEC is a quantity of first interest when designing IEMs as other membrane key properties such as swelling, ionic conductivity and crossover are highly dependent on the IEC.[19–22] The higher the concentration of fixed charged groups and the membrane swelling, the greater the IEC and, generally, the higher the membrane conductivity. A tradeoff thus exists between the membrane conductivity and selectivity due to the swelling of the polymer matrix. The maximum IEC of a polymer membrane corresponds to the amount of fixed charged groups per gram of dry membrane but this metric can be affected by the chemical environment surrounding the ion exchange groups and the counter-ion to be exchanged. Due to the drastic difference in the nature of the counter-ions (i.e. size, hydrophobicity) and in the interaction between the IEM matrix and the solvent used for the exchange (i.e. solvent uptake, hydrophobicity), we decided to study the IEC of commercial membranes in conditions that are relevant for NAqRFB application.

IEC: aqueous vs non-aqueous characterization methods.—Traditionally the IEC of IEMs is determined by acid-base titration methods that rely on ion-exchange in aqueous solutions such as H^+ or Na^+ for cation exchange membranes and OH^- or Cl^- for anion exchange membranes.[19,20,22–27] Additionally, spectroscopic techniques are also employed to determine the IEC.[22,28] Previous research[23,29,30] already highlighted the influence of experimental conditions (i.e., ion size, ion hydrophobicity) on the apparent IEC. Despite this, most of the NAqRFBs literature reports IECs determined in aqueous conditions with hydrophilic ions despite the use of IEMs in organic solvents with hydrophobic ions (e.g., TBA^+, TEA^+, PF_6^-, BF_4^-).[31–33] These approaches give IEC values not representative of the actual application conditions. The determination of the true IEC in non-aqueous systems requires specifically developed analytical tools as currently, no objective standard is available. The intrinsic low coordination tendency of the ions involved in NAqRFBs precludes the use of chemical or redox titration methods and determination of the IEC for non-aqueous systems demands more sophisticated techniques. Spectroscopic methods, such as quantitative fluorine NMR (^{19}F q-NMR), have proven to be useful methods for the identification of fluorine-containing substances.[34,35] ^{19}F q-NMR offers high sensitivity and a wide range of chemical shifts, facilitating the signal quantification and deconvolution of fluorinated polyatomic anions commonly used in NAqRFBs such as PF_6^-, BF_4^-, FSI^- or $TFSI^-$.[36] It is worth noting that other methods such as inductively coupled plasma, atomic absorption spectroscopy or ion chromatography are theoretically valid approaches to tackle this problem but necessitate extensive hardware adjustments when changing the solvent of the analyte.

Operando monitoring of redox active species transport.—Monitoring of the redox active species concentration within the RFB is of prime interest as it gives access to important physicochemical properties of the electrolyte. The electrolyte state of charge (SOC) is one of them and represents the current proportion of the redox active molecules that are still available for energy conversion.[37] Another important parameter determining the RFB performance is the crossover rate of the redox active species through the membrane, which is typically assessed with ex situ setups and only rarely studies focus on understanding transport phenomena through membranes in representative RFB operation conditions.[38–43] The presence of a flowing electrolyte and an applied electric field coupled with high redox active species concentrations affects transport phenomena through the membrane (e.g., membrane selectivity).[44] Upon the available *operando* tools able to probe redox active species concentration in NAqRFBs, voltammetry is of special interest due to the versatility and simplicity of the technique. Instead of using macroelectrodes, we use microelectrodes to obtain reliable signals. Voltammetry at microelectrodes is selective towards redox active materials in solution, minimizing interferences from other redox inactive compounds present in the supporting electrolyte which can be a challenge with classical spectroscopic methods (i.e., UV–vis, NMR, IR). The micrometric dimensions of such electrodes lead to a steady-state diffusion-limited current plateau, facilitating the quantification of redox active molecules in solution compared to traditional macroelectrodes.[45–48] Finally, the use of microelectrodes in organic media is advantageous thanks to their negligible charging currents, high mass transport rates and reduced ohmic drop making them particularly suitable to measure highly concentrated electrolytes typically used in NAqRFBs.[45,46,48–50] Most of the literature focused on using microelectrodes to study RFBs state-of-charge and redox active molecules decay but here we implement microelectrodes to study membrane transport phenomena in NAqRFBs in *operando* conditions.[45,50,51]

Objectives of this work.—In this work, we present two methods to be added to the portfolio of membrane characterization methods for NAqRFB applications: the IEC and the crossover rate in NAqRFBs and Fig. 1 shows a schematic representation of the integration of those two methods in a redox flow battery. We focus on these two metrics, covering two distinct knowledge gaps, and deliberately exclude membrane resistance as much work on this topic has been carried out.[52] In the first part of the paper, we propose

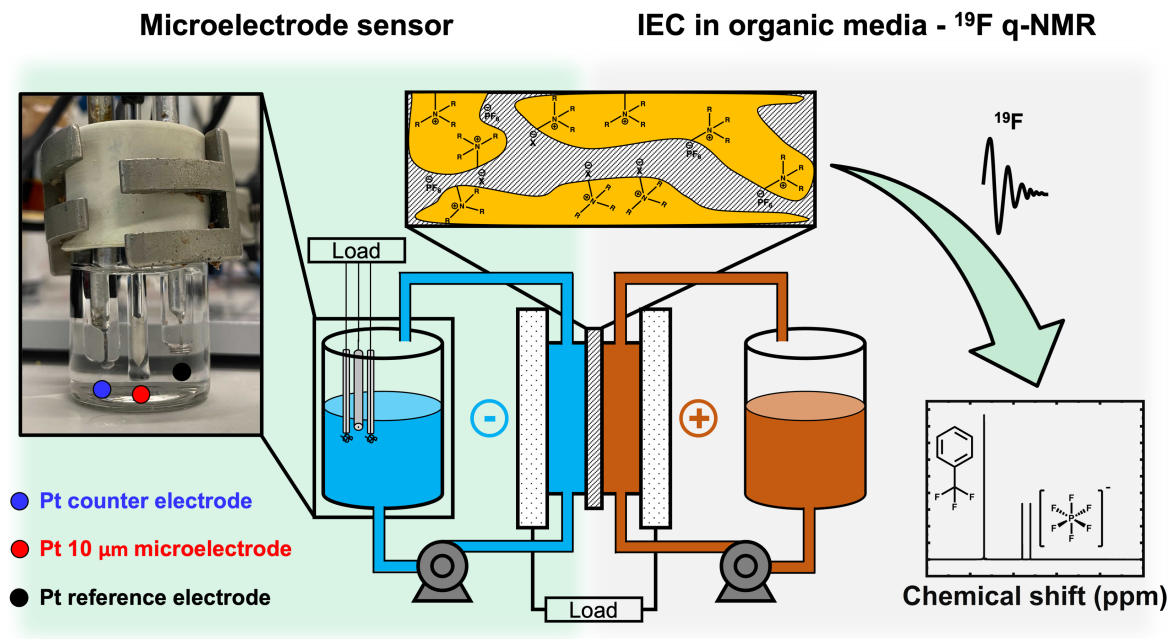

Figure 1. Integration of advanced characterization methods to study NAqRFBs. Photograph of the three-electrode setup positioned in the electrolyte tank: WE (Pt microelectrode 10 μm diameter), RE (Pt wire 0.5 mm diameter), CE (Pt wire 0.5 mm diameter). IECs of fluorinated ions widely used in NAqRFBs were determined by quantitative ^{19}F-NMR using α,α,α-trifluorotoluene as internal standard.

a methodology to assess the IEC of commercial anion exchange membranes by using ^{19}F q-NMR as highly selective quantification tool. This methodology is intended to pave the way towards a fuller understanding of ion exchange dynamics in organic media to possibly foster a faster development of NAqRFBs. In the second part, we use microelectrodes to determine quantitatively the crossover rate of 2,2,6,6-tetramethylpiperidine-1-oxyl (TEMPO) through commercial IEMs and porous separators under fluid dynamic conditions mimicking real NAqRFB operation. We show that integrating microelectrode in the electrolyte tanks not only enables crossover determination but also permits dynamic determination of electromigration of the redox active species and battery SOC.

Experimental

Materials.—All ion exchange membranes as well as porous separators were purchased from commercial sources, specifically Nafion 212 and Nafion 211 (FuelCellStore), Fumasep FAP450 (FuelCellStore), Neosepta AHA and AFX (Eurodia). The porous separators used were Celgard 2500 (Celgard) and Daramic®175 (Daramic®). An overview of the used membranes can be found in Table I.

The chemicals used were tetra-n-butylammonium hexafluorophosphate ($TBAPF_6$) (98%, Alfa Aesar), tetra-n-butylammonium tetrafluoroborate ($TBABF_4$) (99%, Alfa Aesar), tetra-n-butylammonium chloride (TBACl) (≥ 97%, Merck), sodium hexafluorophosphate ($NaPF_6$) (99%, Fisher Scientific), sodium tetrafluoroborate ($NaBF_4$) (≥97%, Fisher Scientific), sodium chloride (NaCl) (100%, VWR), anhydrous α,α,α-trifluorotoluene (TFT) (≥97%, Merck), acetonitrile (Merck), dry acetonitrile in the glovebox (99.9%, Acros Organics), silver nitrate ($AgNO_3$) (Sigma-Aldrich), and TEMPO (98%, Sigma-Aldrich), all the chemicals were used as received. $TEMPO^+PF_6^-$ was synthesized by chemical oxidation with nitrosonium hexafluorophosphate ($NOPF_6$) (96%, Thermo Scientific) in a glovebox (MBraun, LABstar, O_2 and H_2O < 0.5 ppm).[6] Methyl viologen (MV^{2+}) was synthesized[53] and recrystallized twice from boiling ultrapure water. Ultrapure water (18 M Ω) was produced with a Elga Purelab Flex water purifier. NMR tubes (Borosilicate glass tube, 5 mm diameter, 0.38 mm wall thickness, Merck) were used to quantify the IECs of the different membranes. All the electrochemical measurements were recorded on a VMP-300 potentiostat (Biologic) and flowrates were controlled with peristaltic pumps (Masterflex). For the flow cell experiments, the flow diffusers were fabricated from polypropylene (McMaster-Carr) and the interdigitated flow fields (IDFF) were milled from a 3.2 mm thick graphite composite plate (G347b-311, MWI, Inc.). In all experiments carbon fiber-based porous electrodes (Freudenberg H23) were used as received, one electrode per half-cell. Teflon gaskets (ERIKS) were used to seal the flow cell ensuring a homogeneous compression of roughly 33% of the electrodes and to define the geometric area (2.55 cm^2) of the cell. The flow cell was compressed to 2 N·m with a torque wrench. Electrolyte solutions were placed in 25 ml glass vials sealed with rubber septa with the electrolyte inlet and outlet

Table I. List of polymer membranes used in this study and dry thicknesses.

Membrane	Abbreviation	Type	Dry thickness (μm)
Celgard 2500	Celgard	Porous separator	25[a)]
Daramic® 175	Daramic®	Porous separator	175
Nafion 212	N212	Cation exchange	50.8[a)]
Nafion 211	N211	Cation exchange	25.4[a)]
Fumasep FAP-450	FAP450	Anion exchange	50
Neosepta AFX	AFX	Anion exchange	120
Neosepta AHA	AHA	Anion exchange	182

a) As reported by the manufacturer.

connected to the peristaltic pump by LS/14 Norprene® tubing (Masterflex). Prior to the flow cell experiments, the pump flowrate was calibrated using pure acetonitrile to account for the pressure drop of the flow cell and keep consistency over the whole experimental campaign.

Determination of ion exchange capacity in different solvents.— Ions can be transported within the structure of an ion exchange membrane by interacting with the fixed charge-bearing groups of opposite charge which concentration is represented by the ion exchange capacity of the polymer membrane. The ion exchange capacity of supporting anions commonly used in organic electrolytes was determined by ^{19}F q-NMR As illustrated in Fig. 2, the ion exchange capacity was determined both in aqueous and non-aqueous conditions by performing ion-exchange in water or in acetonitrile, respectively.

Aqueous exchange was carried out by exchanging weighed (∼0.2 to 0.3 g) and dried commercial membranes in 20 ml of 1 M $NaPF_6$ or $NaBF_4$ dissolved in ultrapure water, in a shaker at 300 rpm for two weeks. The membranes in PF_6^- or BF_4^- forms were then rinsed with 100 ml of pure solvent three times and dried with a tissue before placing them in a precisely measured volume (10 ml) of 1 M NaCl for aqueous exchange or 1 M TBACl for non-aqueous exchange. The membranes in NaCl or TBACl solutions were placed in the shaker at 300 rpm for 4 successive baths of 24 h. The membranes were always rinsed with pure solvent and dried with a tissue paper to avoid any ions or solvent contamination between each bath. 0.5 ml were then sampled from each bath and placed in 2 ml gas chromatography vials prior to adding a known quantity of internal standard. For aqueous ion-exchange, NaF was used as internal standard while for non-aqueous ion-exchange TFT was employed. We validate our quantitative ^{19}F-NMR analytical method by analyzing solutions of known concentrations over the course of 10 days (Fig. S1 (available online at stacks.iop.org/JES/169/080528/mmedia)).

NMR spectra were recorded at ambient conditions on a Bruker FT-NMR spectrometer AVANCE III HD-Nanobay (400 MHz, Bruker Ultrashield magnet, BBFO Probehead, BOSS1 shim assembly) in non-deuterated solvents. Each spectrum was recorded with the following parameters: TD = 1310720, NS = 16, DS = 4, SWH = 89285.711 Hz, FIDRES = 0.136239 Hz, AQ = 7.3400321 s, RG = 199.1, DW = 5.600 μs, DE = 6.50 μs, TE = 298 K, D1 = 30.0 s, SF01 = 376.479533 MHz.

[α,α,α-trifluorotoluene] + [PF_6^-] ^{19}F NMR (376 MHz, MeCN) δ/ppm −62.3 (s, F^{CF3}), −72.6 (d, J_{PF} = 706.20 Hz, F^{PF6}). Integration regions: [−61.0 to −63.5 ppm], [−69.0 to −71.6 ppm] and [−71.6 to −74.0 ppm].

[α,α,α-trifluorotoluene] + [BF_4^-] ^{19}F NMR (376 MHz, MeCN) δ/ppm −64.0 (s, F^{CF3}), −152.0 (F^{BF4}). Integration regions: [−61.0 to −67.5 ppm] and [−147.5 to −157.5 ppm].

[NaF] + [PF_6^-] ^{19}F NMR (376 MHz, H_2O) δ/ppm −119.9 (F^F), −72.0 (d, J_{PF} = 706.20 Hz, F^{PF6}). Integration regions: [−70.0 to −72.0 ppm], [−72.0 to −743.0 ppm] and [−115.0 to −125.0 ppm].

[NaF] + [BF_4^-] ^{19}F NMR (376 MHz, H_2O) δ/ppm −120.7 (s, F^F), −150.8 (F^{BF4}). Integration regions: [−115.0 to −125.0 ppm] and [−145.0 to −155.0 ppm].

The PF_6^- concentration in the NMR tube was calculated using Eq. 2[54] where M refers to molar concentration, I is the integral and N is the number of nuclei giving rise to the signal ($N_{PF_6^-}$ = 6 and $N_{standard}$ = 3).

$$M_{PF_6^-} = M_{standard} \bullet \frac{I_{PF_6^-}}{I_{standard}} \bullet \frac{N_{standard}}{N_{PF_6^-}} \quad [2]$$

The PF_6^- or BF_4^- concentration in the ion exchange bath is recalculated from the NMR tube concentration by applying the dilution factor corresponding to the volume sampled from the bath and the volume of solvent used for the NMR analysis. The final membrane IEC is calculated by summing the moles of PF_6^- or BF_4^- exchanged in all the baths and normalizing it by the dry weight of the membrane obtained after drying the membranes at 80 °C under 5 mbar vacuum for 12 h.

Measurement of redox active species concentrations.—In the second part of this paper, we use a microelectrode-based sensor to extract crossover rate of redox active species by measuring steady-state current during voltammetry experiments. As this is not a standard membrane characterization tool, we first give a short theoretical background on this topic, then we describe the sensor setup and experimental validation. Finally, we detail the experimental procedures used to extract various RFB metrics (i.e., SOC, electromigration, membrane crossover rate). We decided to add schematics of each experimental setup in the results and discussion section to ease the understanding of the experimental conditions.

Microelectrode Theory

Microelectrodes are electrodes that feature at least one dimension in the micron scale and have several advantages over classical macroelectrodes. Smaller electrodes lead to higher current densities because of a higher contribution of radial diffusion (at the electrode edges) with respect to planar diffusion (at the electrode center). Another advantage of microelectrodes lies in their ability to probe localized changes in concentrations, giving better insights in transport phenomena than their macro counterpart. Further, microelectrodes show a reduced non-faradaic current contribution corresponding to the formation of a charging current due to the formation of an electrical double layer with respect to faradaic events. The latter not only improves the signal-to-noise ratio but also

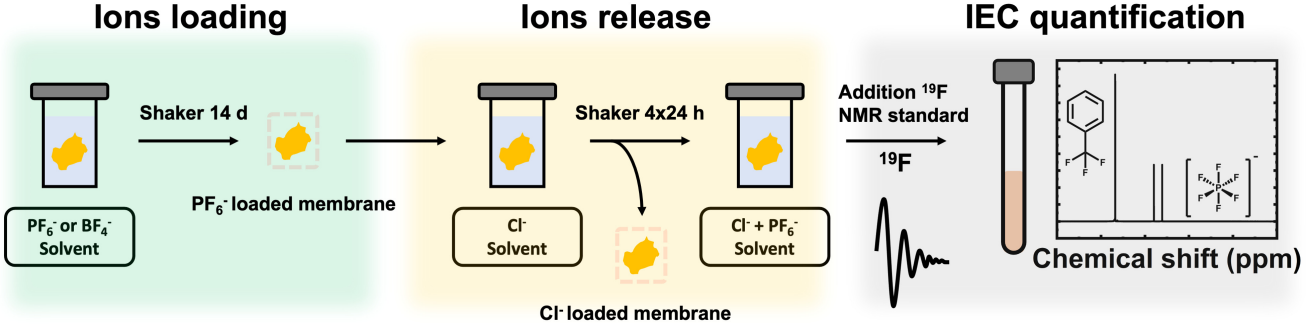

Figure 2. Determination of IEC of hydrophobic anions of anion exchange membranes using ^{19}F q-NMR The fluorinated ions were loaded in the IEMs over the course of 14 days by immersion in a solution combining the desired solvent/ion. The loaded fluorinated ions were then released by chloride ion replacement and subsequently back-titrated using quantitative ^{19}F-NMR with α,α,α-trifluorotoluene as internal standard for non-aqueous exchange conditions or with NaF for aqueous exchange conditions.

results in a faster cell response. Finally, the small critical dimensions of the microelectrodes proved to be of high interest to study electrolytes with low ionic conductivities such as non-aqueous solvents. Microelectrodes operate at much smaller currents (∼nA) than macroelectrodes (∼mA) which generate ohmic drops in the order of hundredths of mV only (in an organic solvent), which is a negligible *iR* distortion. All the advantages of microelectrodes make them highly attractive to measure a large range of active species concentrations in non-aqueous electrolytes typically used in RFB applications, something that cannot be accurately done using macroelectrodes. Therefore, microelectrodes are highly suited to quantify Faradaic reaction in liquid phase.

We consider here a basic faradaic event consisting of a basic charge transfer reaction:

$$O + ne^- \rightleftharpoons R \quad [3]$$

where O and R stand for oxidized and reduced species and ne^- corresponds to the number of electrons involved in the redox reaction between O and R. The redox potential $E_{O/R}$ of the charge transfer reaction between R and O can be calculated using Nernst equation (Eq. 4):

$$E_{O/R} = E^{\circ}_{O/R} + \frac{RT}{nF}\ln\frac{a_O}{a_R} \quad [4]$$

Where $E^{\circ}_{O/R}$ (V) is the redox potential for the couple O/R in standard conditions, R (J K^{-1} mol^{-1}) is the gas constant, T (K) is the absolute temperature, F (C mol^{-1}) is the Faraday's constant, and a_O/a_R correspond to the activity coefficients of the oxidized and reduced species.

If we only focus on the oxidation event associated with Eq. 3: from the moment the microelectrode potential is swept to values more positive than $E_{O/R}$, an anodic current (positive current) will flow at the microelectrode due to the oxidation of R. To sustain the oxidation reaction at the microelectrode, the counter-electrode should host a reduction reaction to keep the electroneutrality within the electrochemical system. If the microelectrode potential is now swept further away from $E_{O/R}$, the oxidation rate of R will increase until a rate-limiting event is reached. If we consider that the redox couple O/R has fast kinetics, then the mass transport of R towards the surface of the microelectrode will become the rate-limiting event and the steady-state limiting current of the system can be measured at the microelectrode. At this point the concentration of R at the surface of the microelectrode approached zero and the steady-state limiting current is determined by the mass-transfer rate of R from the bulk of the electrolyte solution to the microelectrode surface. The steady state limiting current at a disk-shaped microelectrode can be calculated using Eq. 5:

$$I_{SS} = 4nFrDC^* \quad [5]$$

Here, I_{ss} is the magnitude of the steady-state current (A), n corresponds to the number of electrons exchanged, F (s A mol^{-1}) is the Faraday's constant, r (m) is the electroactive radius of the microelectrode, D (m^2 s^{-1}) and C^* (mol m^{-3}) are the diffusion coefficient and the bulk concentration of the considered active species, respectively. The steady state current at microelectrode can also have a Cottrellian contribution depending on the electrode dimensions and the timescale of the experiments. In the present study, we expect a Cottrell current contribution of less than 1% of the total current measured at the microelectrode.

An important practical aspect to consider when working with microelectrodes is the accessibility of the active species to the surface of the microelectrode. As opposed to macroelectrodes, the micron-sized critical dimension of microelectrodes makes them prone to surface fouling when exposed for long times to electrolyte solutions. A simple chemical cleaning might be sufficient to recover the surface of the microelectrode but in case of irreversible fouling, polishing of the microelectrode is needed. The polishing of microelectrodes is particularly important when one want to extract quantitative data from microelectrode measurements. Special care must be taken to always polish the microelectrode surface using mild conditions (e.g., gentle polishing with very fine alumina or diamond suspensions). Aggressive polishing of the microelectrode surface can generate a rough surface that would drastically change the value of steady-state currents. New calibrations will therefore be needed to use the microelectrode quantitatively.

Microelectrode Sensor Construction

Redox active species concentrations were extracted from current measurements at a 10 μm diameter Pt disc microelectrode (BASI) polished to a mirror finish using alumina slurry of 5, 0.3 and 0.05 μm diameter on a cloth polishing pad (PINE Research). Due to extended utilization time of the 3-electrode sensor and, since accurate potential measurements with this electrode were not required, a Pt quasi-reference electrode was employed to avoid any contamination of the electrolyte solution with silver salts or clogging of the frit of traditional silver-ion reference electrode. The counter and reference electrodes were fabricated in-house and consisted of a 0.5 mm diameter Pt wire (99.95%, Thermo Scientific) connected to a sealed hollow glass tube. The glass tube was filled with melted solder Sn60/Pb40 (RS Pro) and a stripped copper cable was plunged in the solder before solidification. The other extremity of the stripped copper cable was a 4 mm diameter banana plug. The same connection type was soldered to the microelectrode to ensure that the working, counter, and reference electrodes did not experience any response instabilities due to contact resistances (Fig. 1, photograph).

Validation of the microelectrode sensor.—As stated above, fouling due to specific adsorption of dissolved species on the microelectrode surface can be problematic, especially for long electrolyte exposure times. We first validated the stability of the applied Pt microelectrode (WE) using two Pt wires of 0.5 mm diameter as counter and pseudo-reference electrodes (CE and RE), under long exposure to TEMPO electrolyte with frequent electrochemical operations (Fig. 3a).

The stability assessment of the microelectrode in TEMPO-containing electrolyte was performed in a single cell configuration (Fig. 3a) to account for the contribution of fluid dynamics on the current response of the microelectrode. In this configuration, the TEMPO electrolyte solution is circulated through a flow cell without potential bias and linear sweep voltammetry (LSV) measurements were performed in the electrolyte tank every 5 min for a total period of 24 h at a scan rate of 50 mV s^{-1}. It is postulated that the TEMPO conversion at the microelectrode has a negligible influence on the total TEMPO concentration in the electrolyte tank. Figure 3b shows that the current response of the microelectrode varied by less than 2%, demonstrating that there is no significant fouling of the microelectrode surface or active species decay during the experiment.

Next, we calibrated the microelectrode at different flowrates with an electrolyte containing pure TEMPO to correlate microelectrode current with TEMPO concentration. The microelectrode steady-state current is here calibrated at different TEMPO concentrations and different flowrates. Calibration curves are shown in Fig. 3c for electrolyte flowrates comprised between 0 and 10 ml min^{-1} and TEMPO concentrations between 0.05 and 0.25 M. We summarize the linear fit results for each flowrate in Table II. We used these correlations to calculate crossover rates through the membranes by converting microelectrode steady-state currents into TEMPO concentrations. The slope of the linear fit of the calibration curves does not vary significantly in the studied range of flowrates. This result might be counterintuitive as the mass transfer of the redox active species towards the surface of the microelectrode is expected to be positively correlated with the electrolyte flowrate due to higher mixing, resulting in higher currents at higher flowrates. This correlation between microelectrode steady-state current and electrolyte linear

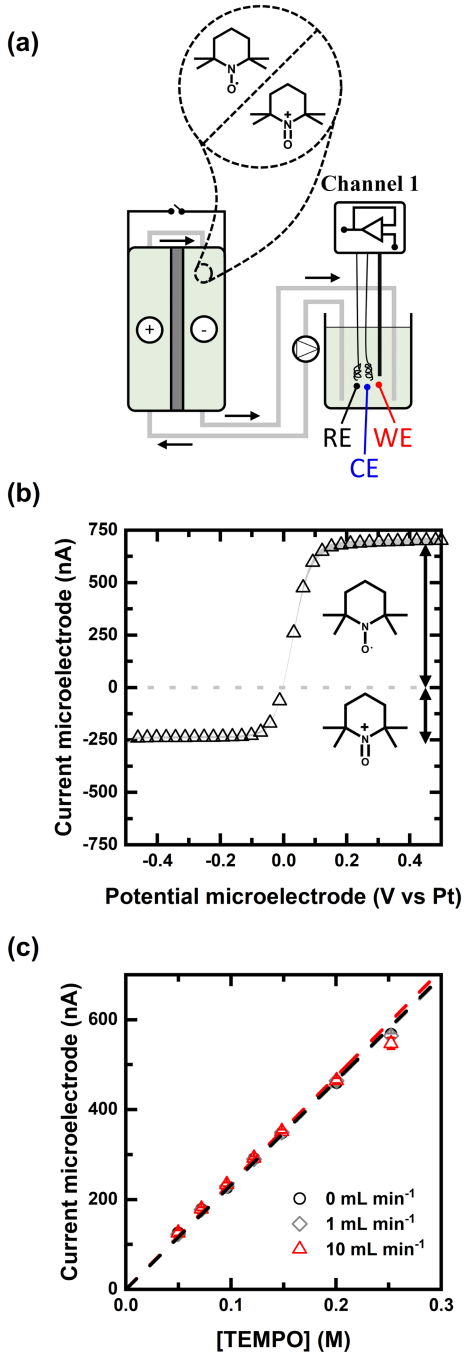

Figure 3. Microelectrode sensor validation and calibration. (a) Schematic representation of the experimental setup. The 3-electrode sensor is placed in the electrolyte tank of a TEMPO single cell electrolyte NAqRFB. Electrolyte mixture: 75% SOC of TEMPO/TEMPO$^+$ in 0.5 M TBAPF6 in acetonitrile (b) microelectrode current stability experiment over the course of 24 h with linear sweep voltammetry recorded every 5 min at 40 ml min^{-1}. The grey area represents one standard deviation for N = 305. The positive currents correspond to electrochemical oxidation of TEMPO to TEMPO$^+$, negative currents correspond to the reverse event. (c) Calibration curves of TEMPO solutions of different concentrations recorded using a three-electrode microelectrode sensor.

velocity has already been studied by Neyhouse et al.[50] These authors found that higher electrolyte velocities resulted in higher steady-state currents at the microelectrode sensor. Their calibration using a flow-through approach showed a steady-state current increase of roughly 55% between 0 and 10 ml min^{-1}, compared to 2.5% in this study. We attribute the differences between the present work and their study to the chosen microelectrode configuration. Our system relies on placing the microelectrode in the electrolyte tank while their sensor is a flow through configuration. Our configuration is aiming to place the microelectrode sensor at the point where the RFB system exhibits the lowest electrolyte linear velocity (i.e., the electrolyte tank), resulting in minimal steady-state current changes upon fluid dynamic variations.

Table II. Linear fitting results of the TEMPO calibration using a 3-electrode sensor. WE (Pt microelectrode 10 μm diameter), RE (Pt wire 0.5 mm diameter), CE (Pt wire 0.5 mm diameter). Electrolyte: TEMPO in 0.5 M TBAPF$_6$ in acetonitrile. For each TEMPO concentration, a total of four LSVs were recorded and averaged (N = 4), the error bars correspond to one standard deviation. The detection limit of our system was estimated from blank measurements (N = 7) and correspond to 0.2 mM.

Flowrate (ml min^{-1})	Slope of the linear fit (nA M^{-1})	R^2
0	2320	0.999
1	2310	0.999
10	2370	0.998

Microelectrode Sensor Applications

Operando state-of-charge and migration monitoring.—A flow cell assembly was connected to two separate tanks, with one tank containing 0.2 M TEMPO in 0.5 M TBAPF$_6$ in acetonitrile and the second containing 0.5 M TEMPO$^+$PF$_6^-$ in 0.5 M TBAPF$_6$ in acetonitrile, both 10 ml. Daramic®175 was used as porous separator and three electrodes Freudenberg H23 (210 μm) were used at each side of the RFB by compressing them between two Teflon gaskets (210 μm). The microelectrode sensor was placed in the tank initially containing 0.2 M TEMPO which was connected to the working electrode of the flow cell. The electrolyte flowrate was 40 ml min^{-1} and ±100 mA was used as charging/discharging current with a potential limit set up at 1 V. Two separate potentiostat channels were used, one was connected to the microelectrode sensor while the other was used to cycle TEMPO vs TEMPO$^+$PF$_6^-$ in the flow battery. LSVs were obtained from −0.5 to 0.75 V (vs Pt) at a scan rate of 50 mV s^{-1} and the value of the steady-state current was determined as the average of the final 25% of the plateau. While the positive currents at the microelectrode correspond to the oxidation of TEMPO to TEMPO$^+$, the negative currents correspond to the reverse reduction event. The amplitude of the linear LSV represent the current difference between the oxidative and reductive current plateaus and is proportional to the total concentration of TEMPO species in the electrolyte. The state of charge can be calculated using Eq. 6:

$$SOC = \frac{I_{oxidation}}{I_{oxidation} + I_{reduction}} \quad [6]$$

Where $I_{oxidation}$ and $I_{reduction}$ correspond to positive and negative currents (nA) attributed to TEMPO oxidation and TEMPO$^+$ reduction, respectively. It is important to note that any shift in the half-wave potential of the redox couple TEMPO/TEMPO$^+$ is attributed to the potential drift of the Pt pseudoreference electrode and does not affect the magnitude of the oxidative and reductive currents.

Crossover determination through commercial membranes.—For the crossover experiments, membranes were first wetted in the blank electrolyte solution for at least one week and kept in a shaker in solution. A cell configuration with two separate tanks was used without any voltage applied to measure the crossover rate of TEMPO through the commercial porous separators and ion exchange membranes. In the case of dense IEMs, three droplets of the blank electrolyte were added during the cell construction to wet the electrodes and avoid membrane drying and curling. A flow cell

assembly was connected to two separate tanks, with one tank containing 10 ml of blank electrolyte (0.5 M $TBAPF_6$ in acetonitrile) and the second tank containing 10 ml of 0.5 M $TBAPF_6$ and 0.3 M TEMPO in acetonitrile. At the blank tank the TEMPO concentration was measured by LSV at time intervals of 2 or 5 min, using the microelectrode sensor. LSVs were obtained from 0.0 to 1.5 V (vs Pt) at a scan rate of 50 mV s^{-1} and the value of the steady-state current was determined as the average of the final 25% of the plateau. Finally, the membrane crossover rate was extracted by fitting the experimental data to the Fick's second law of diffusion solved as (Eq. 7):

$$C_{t,x} = C_{t=\infty} + (C_{t=0} - C_{t=\infty})e^{\left(\frac{-D\ A\ t}{Vx}\right)} \quad [7]$$

Where $C_{t,x}$ (mol l^{-1}) is the concentration of TEMPO at the initially TEMPO-free side in time, D is the diffusivity (cm^2 s^{-1}) which is the fitting parameter, A (cm^2) is the membrane area, t is the time (s), V (ml) is the volume of electrolyte in the initially TEMPO-free side, $C_{t=\infty}$ (mol l^{-1}) is the maximum TEMPO concentration reached in the initially TEMPO-free side and $C_{t=0}$ (mol l^{-1}) is the concentration of TEMPO in the initially TEMPO-free side and is equal to zero. We extracted the TEMPO diffusivity in different commercial membranes by fitting experimental results to Eq. 7.

Electrochemistry at microelectrode in concentrated electrolyte.—In practice, RFB systems use two different redox active species each of them in the form of at least two distinct oxidation states (except if SOC = 0 or 100%). Active species crossover result in capacity fade overtime and a possible strategy to minimize the cell capacity fade is to use premixed electrolytes to lower the concentration-gradient-driven crossover.[18] In this experiment, we aim to assess the applicability of microelectrodes in pure and mixed systems and understand the limits of traditional calibration curves for active species concentration determination. We used TEMPO as catholyte while methyl viologen was employed as anolyte material, both redox molecules are chosen for their stability, availability, and ease to synthesize. A flow cell assembly was connected to a single tank, Daramic®175 was used as porous separator and three electrodes Freudenberg H23 (210 μm) were used at each side of the RFB by compressing them between two Teflon gaskets (210 μm). The single cell was not polarized and LSVs were performed on solutions containing either only TEMPO, only methyl viologen or a mixture of both in 0.2 M $TBAPF_6$ in acetonitrile at different concentrations and at a scan rate of 50 mV s^{-1}. LSVs were recorded using a three-electrode setup placed in the electrolyte tank: WE (Pt microelectrode 10 μm diameter), RE (Pt wire 0.5 mm diameter), CE (Pt wire 0.5 mm diameter). Additionally, the steady state currents were extracted, and calibration curves were constructed by linear fit of the experimental data for each tested flowrate (5, 10 and 20 ml min^{-1}).

Results and Discussions

Ion-exchange capacity of commercial anion exchange membranes.—We carry out exploratory work on the dynamics of ion-exchange involving common anions used in NAqRFBs, specifically PF_6^- and BF_4^-, and compare IECs of those ions to values determined with conventional ions used in aqueous chemistries. Figure 4 and Table III show the IECs of three commercial anion exchange membranes ion-exchanged for two weeks in PF_6^- or BF_4^- electrolytes (in water or acetonitrile) and then subjected to different 24 h chloride baths to release the fluorinated ions. Firstly, we find that all the IEC values are significantly lower than values reported in literature or by the manufacturer (Table III) using traditional aqueous anions (e.g., OH^- or Cl^-).

Secondly, IECs reported for PF_6^- anions are consistently lower than for BF_4^- regardless of the membrane or solvent used. We hypothesize this observation being a consequence of the lower charge density and larger size of PF_6^- anion, resulting in weaker interactions with the different ion exchange sites of the IEMs[58,59] Finally, the ion exchange process in water (Figs. 4a, 4c) is slower than when carried out in acetonitrile as shown by the absence of PF_6^- or BF_4^- anions in solution after the first ion exchange bath (Figs. 4b, 4d and S2–S19).

Table III. Utilization (% of aqueous IEC) of the IEC of the different commercial membranes with PF6- and BF4- anions in water or acetonitrile. The interval of accessible ion exchange capacity is estimated based on IEC determination in aqueous conditions reported by the supplier or in the literature, considered as the maximum ion-exchange capacity of each membrane. Reported intervals were 1.15–1.25 for AHA, 1.5–2 for AFX and 1.2–2.18 for FAP450.[55–57]

	Accessible IEC (%)			
	H_2O		MeCN	
Membrane	PF_6^-	BF_4^-	PF_6^-	BF_4^-
AFX	37–50	66–88	26–34	45–60
AHA	32–35	60–65	44–44	79–86
FAP450	8–15	35–65	5–10	17–31

To the best of our knowledge, no dedicated study has focused on elucidating the impact of the type of ion on the IEC of anion exchange membranes in different solvents. Nevertheless, we use previous knowledge of ion exchange resins and their application in ion chromatography to contextualize our results. First, we compare the timeframe of our experiments to traditional IEC determination methods (e.g., acid-base titration, elemental analysis, etc.) to assess the kinetics of the ion exchange process with fluorinated ions. Karas et al.[22] compared theoretical IECs with experimental values from traditional methods and reached IECs close to the theoretical values for ion-exchange times in only 12 h. In our case even after 96 h of ion exchange with refreshing of the solution every 24 h we could not reach this theoretical IEC value though. Our results reveal both a slow ion exchange rate and a partial inaccessible IEC when using fluorinated ions. This has important implications on the actual RFB performance and on the development of future membrane materials for NAqRFBs.

Heterogeneous ion exchange processes are rather complicated and depend on a multitude of parameters such as the ion association and the solvation of the free ions in solution and the charged groups of the IEM, the hydrophilicity of the matrix bearing the charged groups, and the type of solvent, among others.[60–63] PF_6^- and BF_4^- are both highly lyotropic and chaotropic anions, meaning they are weakly hydrated and can disrupt the natural hydrogen bond network of water without ordering water molecules around them.[58,61,64,65] Additionally, electrolyte uptake experiments were performed to assess the solvation state of the membranes (Fig. S20). The results show that all the membranes have higher electrolyte uptake in MeCN, accompanied by larger membrane dimensional swelling propensity. Assuming a higher accessibility to the anion exchange membrane charge-bearing groups in a swollen membrane, a higher swelling in MeCN would result in higher IECs in MeCN. However, we observe the opposite trend. FAP450 exchanged in $TBABF_4$ in acetonitrile is a striking example as the sample displays the higher electrolyte uptake and the lowest IEC. Electrolyte uptake experiments only account for the macroscopic solvation of the membrane material and do not provide information on the local solvation state of the charge bearing groups present in the membrane. This result stresses the intricate influence of the nature of the solvent, the exchanged ions, and the membrane charge-bearing groups on the interactions between the latter and their counter-ions. The fast ion release in MeCN can be attributed to the higher hydrophobicity of the solvent compared to water. Similar trends have been observed in ion chromatography with a decrease in the retention time of PF_6^- and BF_4^- when the proportion of MeCN in the mobile phase is increased, indicating a higher affinity of PF_6^- and BF_4^- for acetonitrile than for water.

One of the simplest strategies to improve battery performance is to reduce the ohmic overpotential contribution coming from the transport of supporting ions through the membrane. Ionic conductivity of IEMs can be increased by molecular engineering, that is by increasing the number of charged bearing groups[66] (i.e., the IEC) enhances the probability of transferring ions through the membrane.[67] A decrease in the accessibility of the charge-bearing groups might be explained either by poor wetting of the polymer matrix in the electrolyte solution or by an increased difficulty for the counter ions to penetrate in the free volumes if the polymer network of the IEM. It is important to point out that in our measurements the only driving force for the ion-exchange was a concentration gradient. Under NAqRFB operating conditions IEMs are also subjected to an electric field that might affect the anion distribution within the IEM structure. Our results highlight that IECs of commercial membranes are consistently lower than theory when characterized in in electrolytes that are meaningful for NAqRFB applications. To fulfil electroneutrality within the ion exchange membrane polymer matrix the charged groups present in the membrane polymer are electrostatically compensated by counter-ions. The only partial exchange of the counter-ions initially present in the membrane for counter-ions of the electrolyte due to steric or electrostatic effects result in mixed-counter-ion membrane. Our observations question the validity of the current experimental approach of characterizing the IEC of a membrane in aqueous conditions while the intended application uses non-aqueous conditions. While being exploratory, this work unlocks a quantification tool that is selective to fluorine-containing chemicals by means of a simple experimental procedure relying on the addition on an internal calibration standard. We envision that this tool could benefit to the development of NAqRFBs through the understanding of the relation between membrane polymer structure and critical membrane properties (i.e., IEC).

SOC and migration.—In the experimental section we demonstrated that a Pt microelectrode could be inserted in one of the electrolyte tanks of a RFB and maintain a stable current response during 24 h. This long-term stability test paves the way to use microelectrode sensors in a polarized RFB to study more complex battery phenomena such as dynamic state of charge monitoring or active species crossover through the membrane. Figure 5a illustrates the experimental setup which is a symmetric cell where we cycle TEMPO vs $TEMPO^+$. The cell voltage during the first polarization half-cycle is presented in Fig. 5b and shows the evolution of a positive cell overpotential associated with the oxidation of TEMPO in the working electrode compartment of the flow cell. Simultaneously, the concentration of TEMPO active species in the WE compartment of the flow battery is quantified by performing linear sweep voltammetry at the microelectrode sensor. The total concentration of TEMPO species is proportional to the amplitude (i.e., the current difference between the higher and lower plateaus of the sigmoid) of the current response at the microelectrode while the deconvolution of TEMPO and $TEMPO^+$ concentrations can be obtained from the contributions of positive and negative currents. Figure 5c shows the current response measured during the first half-

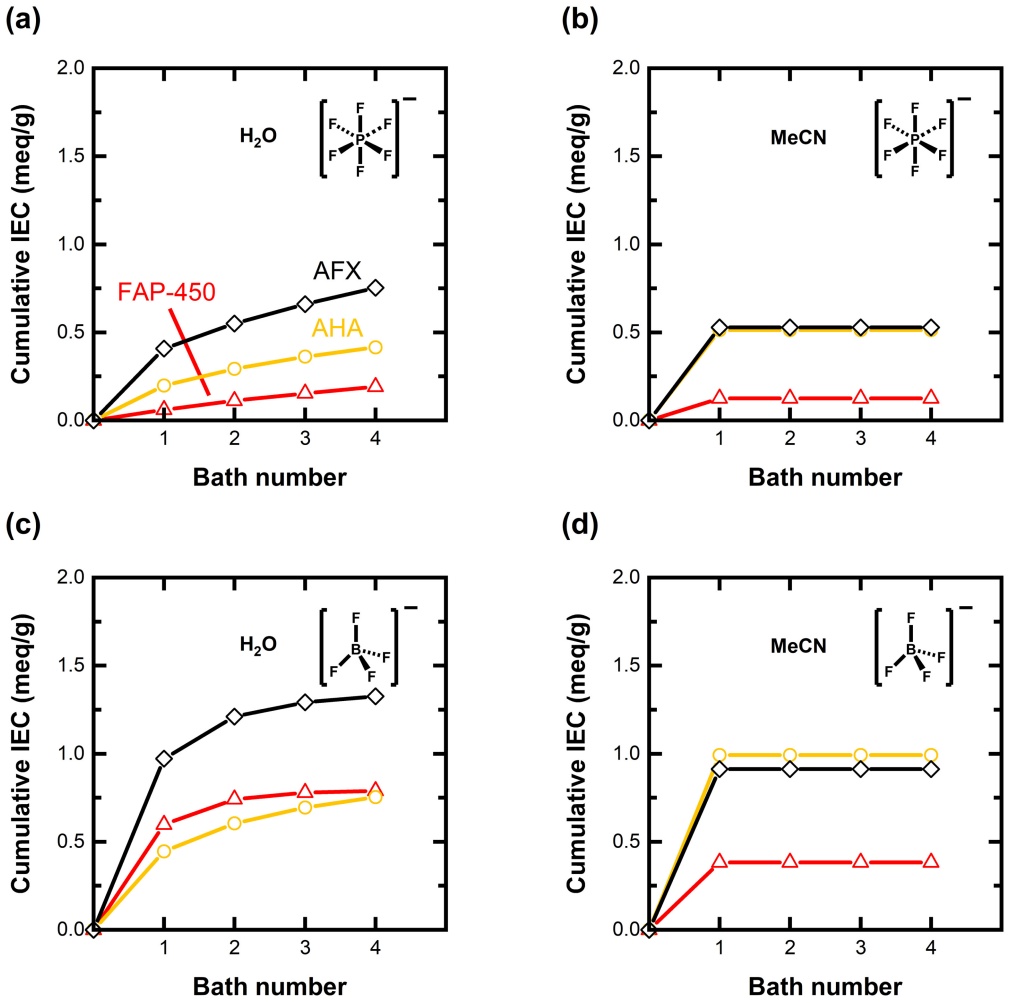

Figure 4. Evolution of the PF_6^- or BF_4^- release dynamics over the course of four baths of 24 h each. All membranes were first exchanged for two weeks in the corresponding PF_6^- or BF_4^- electrolytes with a concentration of 1 M of fluorinated ions. (a) PF_6^- exchange in H_2O and (b) in MeCN. (c) BF_4^- exchange in H_2O and (d) in MeCN. All the fluorinated ions concentrations were determined using ^{19}F-NMR with internal standard.

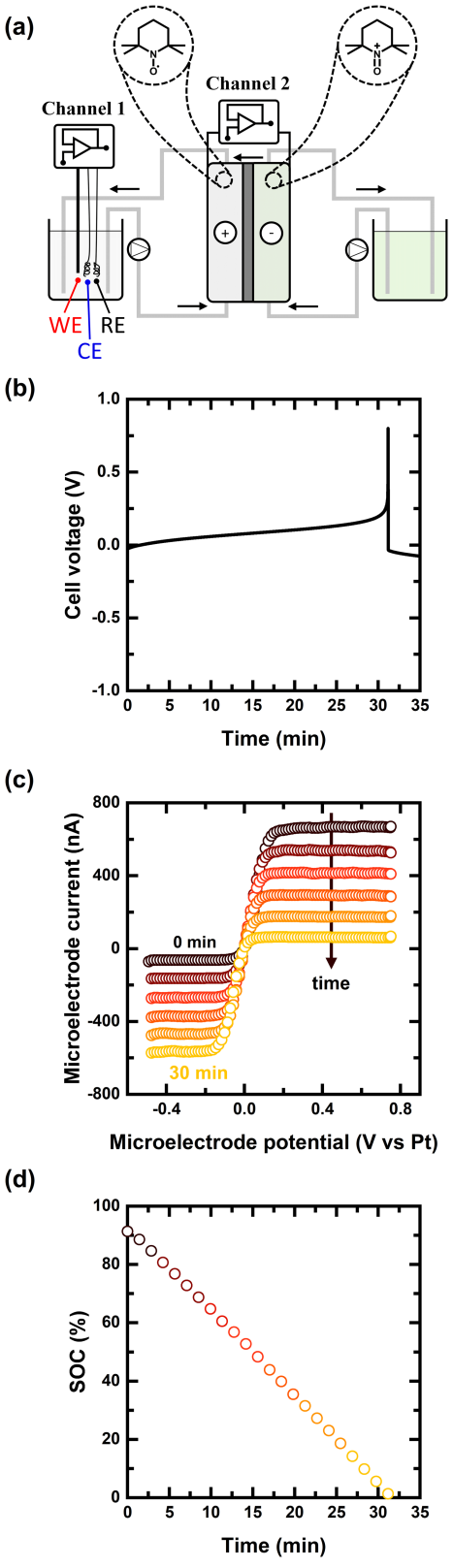

Figure 5. SOC monitoring during cycling of TEMPO vs $TEMPO^+$ in a RFB model cell. (a) Schematic representation of the experimental setup. (b) Cell voltage of the NAqRFB during the first half-cycle. (c) Current recorded at microelectrode place in the WE compartment of the battery and (d) calculated SOC. A charging current of 100 mA was used with a Daramic175 separator. The WE of the battery was in contact with 0.2 M TEMPO in 0.5 M $TBAPF_6$ and the CE with 0.5 M $TEMPO^+PF_6^-$ in 0.5 M $TBAPF_6$.

cycle at the microelectrode placed in the electrolyte tank which initially only contains TEMPO. The battery SOC can be extracted from the oxidative and reductive current contributions at the microelectrode sensor by using Eq. 6 and is plotted in Fig. 5d.

During the first half-cycle a positive current is applied at the WE of the cell which only contains TEMPO and the voltage response of the system is displayed in Fig. 5b. When the current was applied to the battery, the cell voltage increases monotonically due to the conversion of TEMPO to $TEMPO^+$. Figures 5c, 5d show the evolution of the current response at the microelectrode during the same half-cycle and a linear conversion of TEMPO to $TEMPO^+$ at a fixed current density is observed. At the end of the experiment, most of the TEMPO has been consumed and only a small positive current contribution remains due to the voltage limit of the experiment. Finally, it is interesting to note that the amplitude of the current measured at the microelectrode significantly decreases throughout the half-cycle, indicating a drop in the total concentration of TEMPO species at the WE of the RFB. Such behavior is unlikely to be due to the diffusion of TEMPO species away from the WE compartment of the RFB as it holds the lowest TEMPO species concentration. To better understand the possible membrane transport phenomena responsible for these observations, we perform LSV at the end of each half charge-discharge cycle and we correlate the current amplitude at the microelectrode with TEMPO species transport through the membrane.

Keeping the same TEMPO/$TEMPO^+$ model system, the studied timeframe is expanded to five half-cycles and the current amplitude in the WE compartment of the battery at the end of each half charge-discharge cycle is recorded. Figure 6b shows the current (red line) and voltage (black line) at the WE of the polarized RFB while the symbols represent the points at which the microelectrode monitored the total current of TEMPO species present in the WE compartment (Fig. 6c). During the first half-cycle TEMPO is oxidized to $TEMPO^+$ at the WE of the RFB which is held at a positive electric potential. $TEMPO^+$ generated at the WE migrates to the CE of the RFB which is held at a negative electric potential while the motion of the neutral TEMPO radical is not affected by the applied electric field. $TEMPO^+$ electromigration from the WE to the CE results in a decrease of the current amplitude measured at the microelectrode. This phenomenon is observed after completion of every oxidative half-cycle (Figs. 6b, 6c diamond symbols) at the WE of the RFB.

When the potential of the RFB is reversed, the electromigration direction of $TEMPO^+$ is reversed and the current amplitude measured at the microelectrode increases. The microelectrode current amplitudes at the end of each half-cycle (diamond symbols) and full cycle (triangular symbols) highlight a continuous increase of the TEMPO species concentration in the RFB working electrode compartment. We attribute this concentration increase to the diffusion of TEMPO species from the CE to the WE compartment of the RFB, driven by the initial difference of the total TEMPO species concentrations.

Crossover of redox active species.—To determine the crossover rate of active species through the membrane, the previously discussed approach can be used combined with the calibration curves of the microelectrode current response. Figure 7a shows the setup used to determine the crossover rate of TEMPO through commercial membranes. Figure 7b plots the TEMPO crossover as a function of time at a flowrate of 10 ml min^{-1} in a non-polarized diffusion cell (i.e., cross over cell with the same architecture as a flow battery). Table IV summarizes the TEMPO diffusion coefficients extracted by fitting the experimental data to Eq. 7. Initially, the TEMPO concentration on the blank side increases at a fast pace as the driving force for TEMPO diffusion through the membrane (i.e., concentration gradient) is highest. As the TEMPO concentration in the initially TEMPO-free side increases, the driving force for TEMPO crossover decreases until the chemical potentials at each side of the membrane are equal and a concentration plateau is reached. Celgard is the thinnest membrane and is the only porous

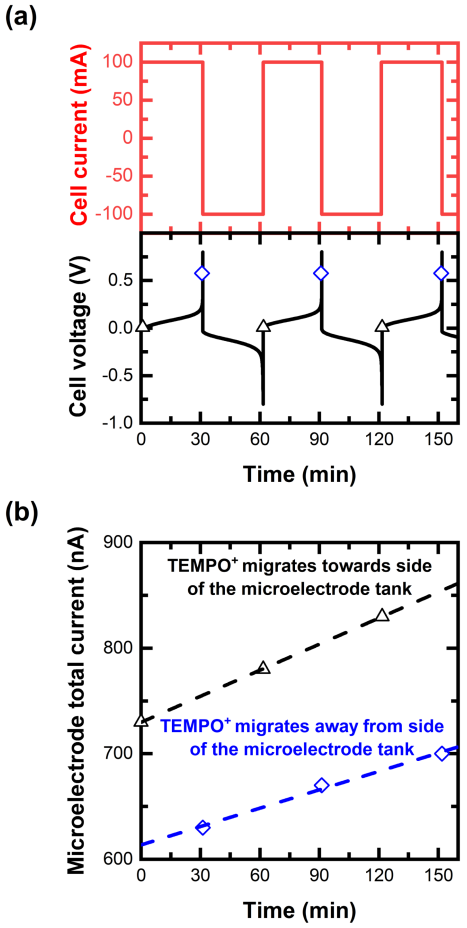

Figure 6. Identifying migration patterns during cycling of TEMPO vs $TEMPO^+$ in a RFB model. (a) Cell current (red line) and voltage (black line) monitored at the working electrode of the RFB. (b) Total amplitude of the current response at the Pt microelectrode at the end of each half-cycle. Symbols represent when the current was recorded at the microelectrode during the RFB cycling. A charging/discharging current of ±100 mA was used with a Daramic175 separator. The WE of the battery was in contact with 0.2 M TEMPO in 0.5 M $TBAPF_6$ and the CE with 0.5 M $TEMPO^+PF_6^-$ in 0.5 M $TBAPF_6$.

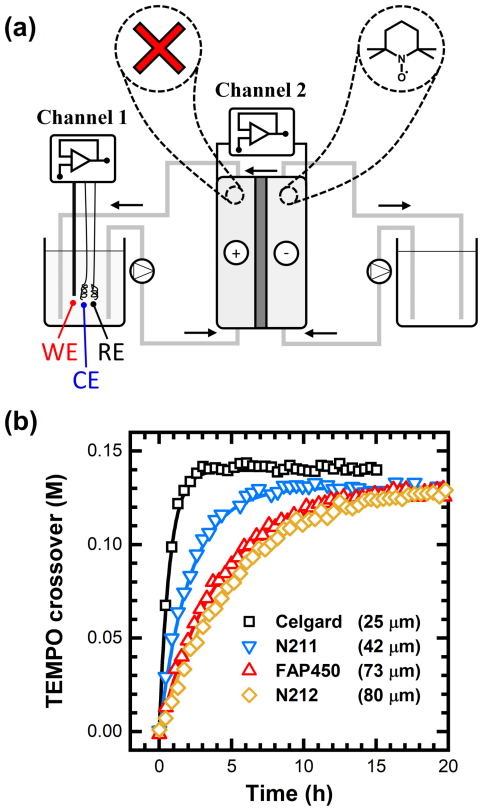

Figure 7. TEMPO crossover characterization in NAqRFB for a set of commercial membranes in acetonitrile. Symbols correspond to experimental data and full lines correspond to a Fickian's diffusion fitting. (a) Schematic representation of the experimental setup. (b) Evolution of the concentration of TEMPO of the initially TEMPO-free side overtime for commercial membranes (symbols) and fitting (lines).

separator of this series, therefore concentration equilibration is fast and requires only three hours. On the other hand, N211 shows concentration equilibration after 10 h while FAP450 and N212 equilibrated after 15 h. These differences in equilibration time are represented by the diffusion coefficients of TEMPO through the various membranes presented in Table IV. The fastest concentration equilibration time observed for Celgard results in the highest diffusion coefficient (i.e., $3.81{\cdot}10^{-6}$ cm^2 s^{-1}) as opposed to N212 that has the shortest concentration equilibration time resulting in the smallest diffusion coefficient (i.e., $1.73{\cdot}10^{-6}$ cm^2 s^{-1}). All dense IEMs reached equilibration at lower concentration values than the only porous separator of this study (i.e., Celgard), we attribute this slight difference to the dilution effect of blank electrolyte added when building RFB to prevent drying and curling of the IEMs. Additionally, FAP450 (positive fixed charge groups) and N212 (negative fixed charge groups) have similar crossover rates (i.e., $1.90{\cdot}10^{-6}$ and $1.73{\cdot}10^{-6}$ cm^2 s^{-1}, respectively). This result highlights that the neutral TEMPO radical is not influenced by the presence of electrostatic charges in the membrane. We rationalize the slightly faster crossover rate through FAP450 to the smaller wet thickness of the membrane compared to N212, bearing in mind that both membranes are fabricated from fluorinated polymers. We use the diffusion coefficient of TEMPO through Celgard 2500 to

Table IV. Experimentally determined TEMPO diffusion coefficient through various commercial membranes. The flow rate was set to 10 ml min^{-1} for these measurements in both compartments.

Membrane	Fitted D (cm^2 s^{-1}) $\times 10^{-6}$
Celgard	3.81
FAP450	1.90
N211	2.16
N212	1.73

evaluate the accuracy of the microelectrode sensor to evaluate transport through membranes. For porous separators, the diffusion coefficient of any species will be influenced by the porosity and the tortuosity of the material and can be calculated using Eq. 8:

$$D_{eff} = \frac{\varepsilon}{\tau} D_{el} \quad [8]$$

Where D_{eff} (cm^2 s^{-1}) is the effective diffusion coefficient of TEMPO through the separator, ε and τ are the porosity and tortuosity of the separator and D_{el} (cm^2 s^{-1}) is the diffusion coefficient of TEMPO in the free electrolyte.[68] Values for Celgard 2500 porosity and tortuosity were previously reported as 0.53 and 1.43 based on X-ray tomographic microscopy analysis.[69] By using Eq. 8 and the experimental diffusion coefficient of TEMPO through Celgard 2500 presented in Table IV, a value of 1.03 10^{-6} cm^2 s^{-1} is obtained for the diffusion coefficient of TEMPO in the free electrolyte. This result is in agreement with previously reported values of TEMPO diffusion coefficient (1.1 10^{-6} cm^2 s^{-1}) in non-aqueous electrolyte of similar composition.[70] This work only focuses

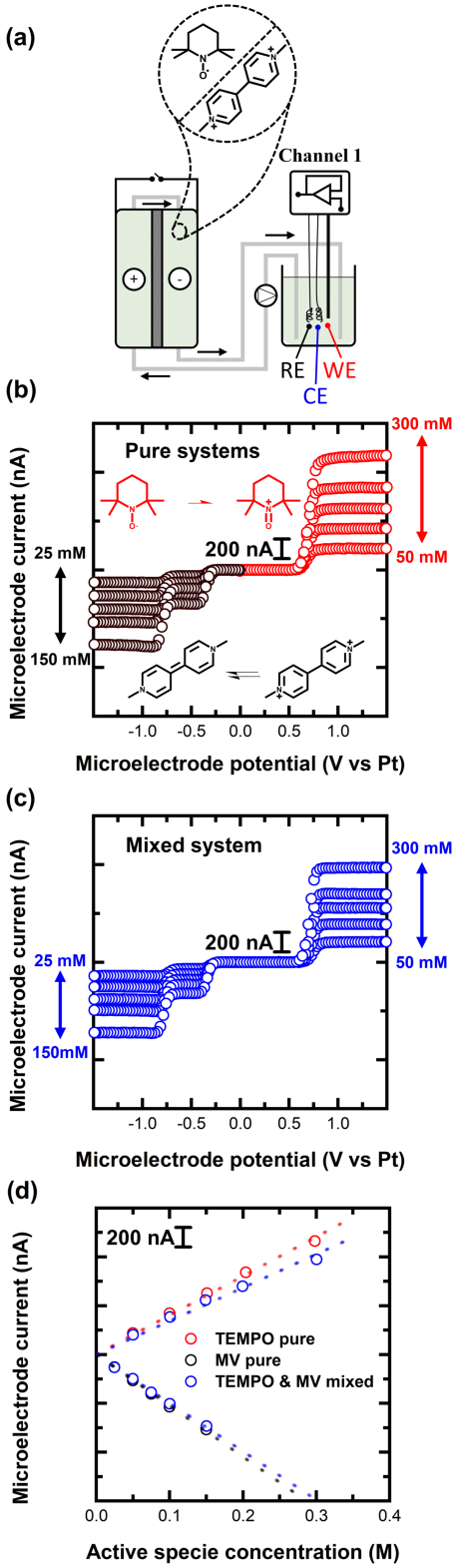

Figure 8. Concentration determination in concentrated electrolytes. (a) Schematics of the experimental setup. LSVs of (b) TEMPO and MV^{2+} in pure electrolytes at an electrolyte flowrate of 20 ml min^{-1} (red symbols corresponding to TEMPO oxidation and black symbols MV^{2+} reductions) and (c) in mixed electrolyte. (d) Calibration curves extracted from LSV analysis. A Daramic175 separator was used with variable concentrations of TEMPO and/or methyl viologen, the supporting electrolyte was 0.2 M $TBAPF_6$ in acetonitrile.

on the determination of crossover rates of a neutral molecule but the hereby developed method can be extended to any redox active molecule. Moreover, we envision that this type of sensor could also be used for the determination of membrane selectivity in electrolytes composed of a mixture of redox active molecules, giving previous information on preferential crossover of certain species. Finally, the simplicity and the compactness of the microelectrode sensor facilitate its use not only for RFB applications but also for other types of electrochemical devices.

Microelectrode sensor in concentrated electrolyte.—Figure 8a shows the experimental setup that is used to obtain calibration curves for electrolytes containing only TEMPO or only methyl viologen (pure systems) or for electrolytes composed by a mixture of both (mixed system). The current response at the microelectrode sensor for active species concentrations between 25 and 150 mM for TEMPO and between 50 and 300 mM for methyl viologen in pure and mixed systems are presented in Figs. 8a and 8c, respectively. From the different LSVs presented in Fig. 8, steady state currents can be achieved at a microelectrode for a single electron transfer event (TEMPO → $TEMPO^+$) as well as for two successive one-electron transfer events (MV^{2+} → MV^+ → MV). For TEMPO, the single electron transfer step is used for calibration, in the case of methyl viologen, the value of the current plateau corresponding to the second one-electron transfer is used to construct the calibration curves. The value of the steady state current plateau for the same active species concentration is consistently lower in the case of a mixed system. This result is also shown in Table V, where smaller values for the calibration slopes are obtained in a mixed systems compared to pure systems with the same concentration of active species. A smaller calibration slope indicates a lower current response at the microelectrode for the same amount of active species, highlighting a lower mass transfer of active species towards the surface of the microelectrode. We attribute this behavior to higher viscous shear forces slowing down active species transport in mixed systems[71] (Fig. S25). Finally, as highlighted in the previous sections and as shown in Table V, the electrolyte flow rate affects only sightly the steady state current measured at the microelectrode with a maximum of 1.1% and 2.84% increase (between 5 and 20 ml min^{-1}) in pure and mixed systems, respectively. From Figs. 8b and 8c it appears that the successive one-electron transfers do not generate the same current as it should be expected for a diffusion controlled heterogenous charge-transfer reaction. This behavior has been studied and reported by Norton et al. and is attributed to migration effects due to low supporting electrolyte concentration.[72] Our results illustrate the limitations of using calibration-based microelectrode sensors in media having a significant change in viscosity during the experiment. We acknowledge that a maximum of 450 mM of active species is still low compared to concentrations recommended for economic viability of NAqRFBs (>1 M)[73] and a proper assessment of the influence of the active species concentration range on the microelectrode steady state current is needed to foster the use of microelectrode-sensors to study membrane transport phenomena.

Conclusions

Non-aqueous redox flow batteries development is still hampered by the poor performance of membranes in organic solvents. Sophisticated characterization techniques for non-aqueous flow batteries must be developed to enable the development of tailored materials with improved performance. We propose quantitative fluorine nuclear magnetic resonance as ex situ method for ion exchange capacity determination of anion exchange membranes with fluorinated anions (i.e., PF_6^- and BF_4^-). Our findings question the validity of the current experimental approach used to characterize the ion exchange capacity of membranes used in non-aqueous electrolytes. The implications

Table V. Linear fit parameters for TEMPO and MV^{2+} systems.

	Pure system				Mixed system			
	Slope of the linear fit 10^{-3} (nA M^{-1})		R^2		Slope of the linear fit 10^{-3} (nA M^{-1})		R^2	
Flowrate (ml min^{-1})	MV^{2+}	TEMPO	MV^{2+}	TEMPO	MV^{2+}	TEMPO	MV^{2+}	TEMPO
5	−5.19	3.98	0.999	0.998	−4.82	3.37	0.998	0.995
10	−5.22	3.97	0.999	0.998	−4.83	3.37	0.998	0.994
20	−5.23	4.02	0.999	0.998	−4.96	3.42	0.999	0.995

behind a partial ion exchange capacity utilization on redox flow battery performance are still unknown, future work should focus on identifying critical ion exchange membrane structure/performance relationships and use this knowledge to design ion exchange membranes that are tailor-made for non-aqueous applications.

In the second part of this work, we successfully implement a simple microelectrode sensor as an additional tool for the characterization of membranes in non-aqueous conditions. We show that different transport phenomena (i.e., diffusion, migration) of redox active species through the membrane along with the battery state-of-charge can be monitored *in operando*. We also developed a method to quantitatively extract crossover rates through polymer membranes in experimental conditions that are relevant for non-aqueous redox flow battery applications. While we demonstrate use for mid-range concentrations of redox active species, we also pinpoint possible challenges when the microelectrode sensor is subjected to highly concentrated electrolytes.

This work opens new perspectives on how to characterize the ion exchange capacity of membranes in organic electrolytes and provides an adequate and simple methodology to quantify redox active species electrochemically driven transport or crossover through membranes.

Acknowledgments

The authors acknowledge the contribution of Marcel van Genderen for providing expertise on the development of the ^{19}F q-NMR methods.

ORCID

Rémy Richard Jacquemond https://orcid.org/0000-0002-4788-2915
Rosa Geveling https://orcid.org/0000-0002-6166-7824
Antoni Forner-Cuenca https://orcid.org/0000-0002-7681-0435
Kitty Nijmeijer https://orcid.org/0000-0002-1431-2174

References

1. S. Chu and A. Majumdar, *Nature*, **488**, 294 (2012).
2. B. Dunn, H. Kamath, and J.-M. Tarascon, *Science*, **334**, 928 (2011).
3. R. M. Darling, K. G. Gallagher, J. A. Kowalski, S. Ha, and F. R. Brushett, *Energy Env. Sci*, **7**, 3459 (2014).
4. C. DeBruler, B. Hu, J. Moss, X. Liu, J. Luo, Y. Sun, and T. L. Liu, *Chem*, **3**, 961 (2017).
5. R. Dmello, J. D. Milshtein, F. R. Brushett, and K. C. Smith, *J. Power Sources*, **330**, 261 (2016).
6. A. Forner-Cuenca, E. E. Penn, A. M. Oliveira, and F. R. Brushett, *J. Electrochem. Soc.*, **166**, A2230 (2019).
7. J. A. Kowalski, L. Su, J. D. Milshtein, and F. R. Brushett, *Curr. Opin. Chem. Eng.*, **13**, 45 (2016).
8. C.-N. Sun, M. M. Mench, and T. A. Zawodzinski, *ECS Meet. Abstr.*, **MA2013-02**, 1694 (2013).
9. M. Zhang, M. Moore, J. S. Watson, T. A. Zawodzinski, and R. M. Counce, *J. Electrochem. Soc.*, **159**, A1183 (2012).
10. C.-N. Sun, M. M. Mench, and T. A. Zawodzinski, *Electrochim. Acta*, **237**, 199 (2017).
11. F. Pan and Q. Wang, *Molecules*, **20**, 20499 (2015).
12. E. Schreiber, R. E. Garwick, M. J. Baran, M. A. Baird, B. A. Helms, and E. M. Matson, *ACS Appl. Mater. Interfaces* (2022).
13. T. Wang, J. Han, K. Kim, A. Münchinger, Y. Gao, A. Farchi, Y.-K. Choe, K.-D. Kreuer, C. Bae, and S. Kim, *Mater. Adv.*, **1**, 2206 (2020).
14. J. Yuan, Z.-Z. Pan, Y. Jin, Q. Qiu, C. Zhang, Y. Zhao, and Y. Li, *J. Power Sources*, **500**, 229983 (2021).
15. F. R. Brushett, J. T. Vaughey, and A. N. Jansen, *Adv. Energy Mater.*, **2**, 1390 (2012).
16. M. Ue, K. Ida, and S. Mori, *J. Electrochem. Soc.*, **141**, 2989 (1994).
17. Y. Huang, S. Gu, Y. Yan, and S. F. Y. Li, *Curr. Opin. Chem. Eng.*, **8**, 105 (2015).
18. Z. Liang, N. H. Attanayake, K. V. Greco, B. J. Neyhouse, J. L. Barton, A. P. Kaur, W. L. Eubanks, F. R. Brushett, J. Landon, and S. A. Odom, *ACS Appl. Energy Mater.*, **4**, 5443 (2021).
19. T. Sata, *Ion Exch. Membr.* (Royal Society Of Chemistry, Cambridge) p. 89 (2007).
20. J. Pan, S. Lu, Y. Li, A. Huang, L. Zhuang, and J. Lu, *Adv. Funct. Mater.*, **20**, 312 (2010).
21. G. Merle, M. Wessling, and K. Nijmeijer, *J. Membr. Sci.*, **377**, 1 (2011).
22. F. Karas, J. Hnát, M. Paidar, J. Schauer, and K. Bouzek, *Int. J. Hydrog. Energy*, **39**, 5054 (2014).
23. F. Helfferich, *Ion Exchange* (Dover Publications, Inc, New York) (1995).
24. E. Alcalde, I. Dinarès, A. Ibáñez, and N. Mesquida, *Molecules*, **17**, 4007 (2012).
25. C. Schmidt, T. Glück, and G. Schmidt-Naake, *Chem. Eng. Technol.*, **31**, 13 (2008).
26. M. Yasukawa, T. Suzuki, and M. Higa, *Membr.-Based Salin. Gradient Process. Water Treat. Power Gener.* (Elsevier, Amsterdam) p. 3 (2018).
27. P. Kumar, R. P. Bharti, V. Kumar, and P. P. Kundu, *Prog. Recent Trends Microb. Fuel Cells* (Elsevier, Amsterdam) p. 47 (2018).
28. P. Naert, K. Rabaey, and C. V. Stevens, *Green Chem.*, **20**, 4277 (2018).
29. H. Deuel, J. Solms, and L. Anyas-Weisz, *Helv. Chim. Acta*, **33**, 2171 (1950).
30. V. K. Gärtner, R. Grießbach, and E. Anton, *Kolloid-Z.*, **175**, 123 (1961).
31. D.-H. Kim, S.-J. Seo, M.-J. Lee, J.-S. Park, S.-H. Moon, Y. S. Kang, Y.-W. Choi, and M.-S. Kang, *J. Membr. Sci.*, **454**, 44 (2014).
32. Y. Li, J. Sniekers, J. C. Malaquias, C. Van Goethem, K. Binnemans, J. Fransaer, and I. F. J. Vankelecom, *J. Power Sources*, **378**, 338 (2018).
33. S. Maurya, S.-H. Shin, K.-W. Sung, and S.-H. Moon, *J. Power Sources*, **255**, 325 (2014).
34. E. Markevich et al., *Electrochem. Commun.*, **15**, 22 (2012).
35. A. V. Plakhotnyk, L. Ernst, and R. Schmutzler, *J. Fluor. Chem.*, **126**, 27 (2005).
36. W. He, F. Du, Y. Wu, Y. Wang, X. Liu, H. Liu, and X. Zhao, *J. Fluor. Chem.*, **127**, 809 (2006).
37. C. Stolze, P. Rohland, K. Zub, O. Nolte, M. D. Hager, and U. S. Schubert, *Energy Convers. Manag. X*, **14**, 100188 (2022).
38. K. Mushtaq, T. Lagarteira, A. A. Zaidi, and A. Mendes, *J. Energy Storage*, **40**, 102713 (2021).
39. E. Wang, E. W. Zhao, and C. P. Grey, *J. Phys. Chem. C*, **125**, 27520 (2021).
40. T. C. Gokoglan, S. K. Pahari, A. Hamel, R. Howland, P. J. Cappillino, and E. Agar, *J. Electrochem. Soc.*, **166**, A1745 (2019).
41. Y. Ashraf Gandomi, D. Aaron, and M. Mench, *Membranes*, **7**, 29 (2017).
42. P. K. Leung, Q. Xu, T. S. Zhao, L. Zeng, and C. Zhang, *Electrochim. Acta*, **105**, 584 (2013).
43. H. Lim, J. S. Yi, and D. Lee, *ChemSusChem*, **12**, 1459 (2019).
44. L. Su et al., *J. Electrochem. Soc.*, **163**, A5253 (2016).
45. J. A. Kowalski, A. M. Fenton, B. J. Neyhouse, and F. R. Brushett, *J. Electrochem. Soc.*, **167**, 160513 (2020).
46. A. J. B. Larry and R. Faulkner, *Electrochemical Methods Fundamentals and Applications* (Wiley, New York, NY) (2001).
47. D. Pletcher, *Microelectrodes Theory Appl.*, ed. M. I. Montenegro et al. (Springer, Dordrecht, Netherlands) p. 3 (1991).
48. R. G. Compton, *Understanding Voltammetry* (World Scientific Publishing) (2018).
49. A. M. Bond, *Analyst*, **119**, 1R (1994).
50. B. Neyhouse, K. Tenny, Y.-M. Chiang, and F. Brushett, *ACS Appl. Energy Mater.*, **4**, 13830 (2021).
51. C. Stolze, J. P. Meurer, M. D. Hager, and U. S. Schubert, *Chem. Mater.*, **31**, 5363 (2019).
52. N. S. Hudak, L. J. Small, H. D. Pratt, and T. M. Anderson, *J. Electrochem. Soc.*, **162**, A2188 (2015).
53. A. J. Downard and M. J. Prince, *Langmuir*, **17**, 5581 (2001).
54. T. Claridge and N. Rees, (2017), Research Document. Department of Chemistry of the University of Oxford (NMR facility). https://nmrweb.chem.ox.ac.uk/Data/Sites/70/userfiles/pdfs/quantitative-nmr.pdf.
55. H. Cho, H. Krieg, and J. Kerres, *Membranes*, **9**, 31 (2019).
56. L. Laín and V. M. Barragán, *Int. J. Hydrog. Energy*, **41**, 14160 (2016).
57. H. Pu, *Polymers for PEM Fuel Cells* (Wiley, New Jersey, NJ) (2014).
58. J. M. Roberts, A. R. Diaz, D. T. Fortin, J. M. Friedle, and S. D. Piper, *Anal. Chem.*, **74**, 4927 (2002).
59. H. Wang, J. Wang, S. Zhang, Y. Pei, and K. Zhuo, *ChemPhysChem*, **10**, 2516 (2009).
60. P. J. Dumont, J. S. Fritz, and L. W. Schmidt, *J. Chromatogr. A*, **706**, 109 (1995).
61. J. S. Fritz, *J. Chromatogr. A*, **1085**, 8 (2005).
62. D. J. Pietrzyk, *Talanta*, **13**, 225 (1966).
63. S. Rabin and J. Stillian, *J. Chromatogr. A*, **671**, 63 (1994).
64. A. Berthod, M. J. Ruiz-Angel, and S. Huguet, *Anal. Chem.*, **77**, 4071 (2005).

65. C. Rutz, L. Schmolke, V. Gvilava, and C. Janiak, *Z. Für Anorg. Allg. Chem.*, **643**, 130 (2017).
66. X. Ye, H. Bai, and W. S. W. Ho, *J. Membr. Sci.*, **279**, 570 (2006).
67. J.-H. Kim, S. Ryu, S. Maurya, J.-Y. Lee, K.-W. Sung, J.-S. Lee, and S.-H. Moon, *RSC Adv.*, **10**, 5010 (2020).
68. M. F. Lagadec, R. Zahn, and V. Wood, *Nat. Energy*, **4**, 16 (2019).
69. D. P. Finegan, S. J. Cooper, B. Tjaden, O. O. Taiwo, J. Gelb, G. Hinds, D. J. L. Brett, and P. R. Shearing, *J. Power Sources*, **333**, 184 (2016).
70. M. J. Baran, M. N. Braten, E. C. Montoto, Z. T. Gossage, L. Ma, E. Chénard, J. S. Moore, J. Rodríguez-López, and B. A. Helms, *Chem. Mater.*, **30**, 3861 (2018).
71. J. B. Cooper and A. M. Bond, *J. Electroanal. Chem. Interfacial Electrochem.*, **315**, 143 (1991).
72. J. D. Norton and H. S. White, *J. Phys. Chem.*, **94**, 6772 (1990).
73. J. Zhang, R. E. Corman, J. K. Schuh, R. H. Ewoldt, I. A. Shkrob, and L. Zhang, *J. Phys. Chem. C*, **122**, 8159 (2018).